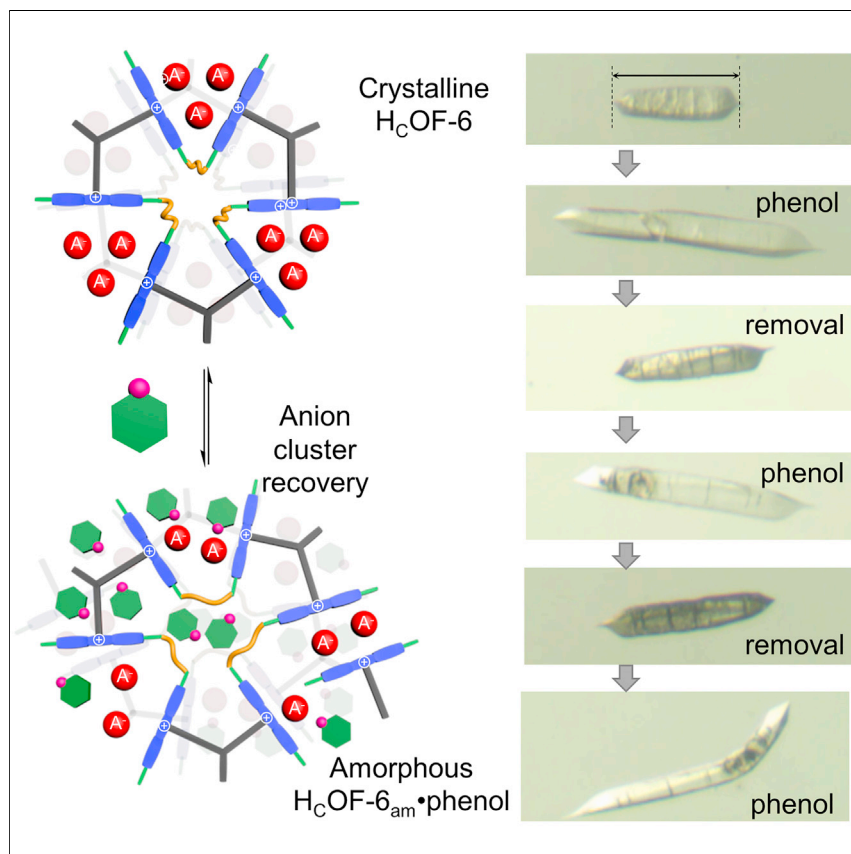


Article

An ultra-dynamic anion-cluster-based organic framework



Bisulfate anion clusters were introduced as soft joints to construct porous molecular crystals, one of which is converted to a single-crystalline hydrogen-bonded cross-linked organic framework H_cOF-6 through photo-irradiated thiol-ene reaction. Upon the uptake and the removal of phenol, the electrostatically repulsive bisulfate anions in the anion cluster of H_cOF-6 were disrupted and reformed, allowing the material to expand and contract rapidly.

Jayanta Samanta, Rick W. Dorn, Wenlin Zhang, ..., Richard J. Staples, Aaron J. Rossini, Chenfeng Ke

wenlin.zhang@dartmouth.edu (W.Z.)
arossini@iastate.edu (A.J.R.)
chenfeng.ke@dartmouth.edu (C.K.)

Highlights

Anion clusters directed formation of porous molecular crystals

SCSC synthesis of a cross-linked organic framework

H_cOF-6 rapidly expand and contract upon phenol uptake and removal

The dynamics of H_cOF-6 comes from the *in situ* (de)formation of anion clusters



Article

An ultra-dynamic anion-cluster-based organic framework

Jayanta Samanta,¹ Rick W. Dorn,^{2,3} Wenlin Zhang,^{1,*} Xuanfeng Jiang,^{1,4} Mingshi Zhang,¹ Richard J. Staples,⁵ Aaron J. Rossini,^{2,3,*} and Chenfeng Ke^{1,6,*}

SUMMARY

Porous organic frameworks that can dynamically expand their voids to guest uptake remain formidable to design. The challenge comes from finding the balance between rigidity and flexibility. Rigidity is required to retain the framework, and the flexibility is needed for reversible expansion/contraction. Herein, we introduced bisulfate anion clusters as soft joints to construct a single-crystalline hydrogen-bonded cross-linked organic framework H_COF-6. Upon the uptake of guest molecules, the anion clusters of H_COF-6 were disrupted, allowing the crystal to expand rapidly (<40 min) to more than twice its original length. Removing these guests restored the anion clusters and the crystallinity of H_COF-6 quickly (<10 min). These guest-induced material size expansions and contractions are highly reversible, and the dynamic anion cluster dissociation-reassociation is confirmed by molecular dynamics simulations and solid-state NMR experiments. The guest-induced size change of H_COF-6 highlights a new approach to synthesize dynamic framework materials by introducing anion clusters.

INTRODUCTION

Dynamic porous crystals that possess responsive framework architectures offer stimuli-responsive sorption and separation capabilities beyond just size-sieving.¹ Featuring adjustable metal-ligand coordination geometries, a group of metal-organic framework (MOF) materials reversibly change their framework geometries upon the sorption of substrates, demonstrating gated sorption^{1,2} and breathing behaviors.^{3,4} Unlike these soft MOFs, it remains nontrivial to trigger guest-gated framework dynamics in crystalline organic framework materials, such as covalent organic frameworks^{5–9} (COFs) or hydrogen-bonded organic frameworks^{10–13} (HOFs). Compared with metal-ligand coordinations, the covalent bond in COFs and hydrogen bonds in HOFs have limited bond rotation capabilities. Therefore, to activate the framework dynamics, the adsorbed guests must possess strong interactions with the framework to compete against the multivalent solid-state packing forces and overcome the energetically demanding covalent bond rotation or hydrogen-bond disruption processes. Most reported dynamic COFs^{14–17} and HOFs^{18–20} are responsive to solvent molecules to maximize the substrate-framework interactions, with one exception is the demetallated amorphous woven COFs,²¹ which enabled large-sized substrate uptake.²² In comparison, hydrogen-bonded cross-linked organic frameworks^{23–25} (H_COFs) that are doubly cross-linked by rigid hydrogen-bonding networks and flexible covalent cross-linkers demonstrated crystalline-to-amorphous framework dynamics upon guest uptake.²⁵ Upon the disruption of the hydrogen-bonded network, the flexible cross-linking moieties in H_COFs

The bigger picture

Porous organic materials possessing dynamic guest sorptions offer better substrate adsorption and separation performance in addition to size-sieving. To date, these dynamic guest uptakes in porous organic materials were primarily discovered through empirical substrate screening. It remains a grand challenge to design and synthesize dynamic organic framework materials with predictable substrate-triggered framework oscillations. In this work, we introduced anion clusters as soft joints to construct porous organic frameworks for highly dynamic substrate sorptions. The synthesized single-crystalline H_COF-6 showed fast size expansions and contractions upon phenol and aniline uptake and removal. Our method paves a path to rationally design porous organic materials with predictable dynamic features, which will enable highly selective substrate sorption, separation, and catalysis for energy-related applications.



allow the framework to expand, thus activating dormant voids to accommodate more guests. However, to achieve the delicate balance between the framework's rigidity and flexibility, tightly bound substrates are still required to disrupt the strong hydrogen-bonded networks in H_COFs. Hence, the development of dynamic porous organic frameworks calls for new synthetic methods to construct robust network architectures with easily accessible framework dynamics.

Here, we present a versatile method to construct H_COF materials with high structural integrity and easily triggered framework dynamics by introducing anion clusters as responsive joints (Figure 1A). A linear monomer (LM, Figure 1C) and a three-arm monomer (TM) consisting of piperazine and diallylmelamine moieties were synthesized to reduce the π - π interactions between stacked layers in the solid state, owing to piperazine's semi-rigid chair conformation. Protonation of the diallylmelamine moieties generated charge-reinforced hydrogen-bonded motifs,¹¹ and the donor-acceptor-donor (DAD) diallylmelamine was converted to donor-donor-donor (DDD) diallylmelaminium (Figure 1B). The assembly of LM with NO₃⁻ or HSO₄⁻ afforded supramolecular polymers with linearly connected anion dimers, whereas TM formed porous single crystals possessing unique tetrakis-anion (HSO₄⁻)₄ and tris-anion²⁶ (HSO₄⁻)₃ clusters at different temperatures. Covalently cross-linking the allyl groups in the preorganized molecular crystal through photo-irradiated thiol-ene single-crystal to single-crystal (SCSC) transformation^{27,28} afforded porous H_COF-6 crystals with (HSO₄⁻)₃ joints (Figure 1D). Compared with the disruption of cation-anion networks, such as guanidinium-,²⁹ ammonium-,³⁰ or amidinium-organosulfonate³¹ HOFs, a considerably smaller energy penalty is required for the disruption of anion dimers³² or clusters due to the electrostatic repulsions between anions. Hydrogen-bond competing substrates, such as phenol and its analogs, demonstrated fast and effective disruption and fragmentation of the anion clusters in H_COF-6, activating the dormant voids to allow for a fast crystal expansion. Removal of the adsorbed phenol in H_COF-6 rapidly contracted the framework and restored the anion cluster joint. Although anion clusters have been investigated in the solid-state supramolecular systems,^{33,34} rarely, if ever, has an anion cluster been introduced to construct a porous network to enable network dynamics upon its association and dissociation. The reversible switching of H_COF-6's network between the crystalline contracted state and the amorphous expanded state bridges the gap between traditional rigid frameworks and swellable cross-linked polymers, providing new opportunities to design porous organic materials that allow the adsorption and separation of substrates beyond just size-sieving.

RESULTS

Of the more than 200 melaminium derivatives reported in the Cambridge Crystal Database, only a few examples³⁵⁻³⁷ demonstrated complementary hydrogen-bonding arrays of melaminium/anion in the solid state. To validate the feasibility of anion (dimer/cluster)-directed assembly of monomers in the solid state, LM was synthesized with two diallylmelamine moieties. A semi-rigid piperazine moiety was introduced to prevent strong π - π stacking between LMs in the solid state.³⁸ We obtained single crystals of LM (Figure 2A, left) through solvent evaporation. The diallylmelamine moieties of LM were hydrogen-bonded in DA-AD fashion, and the piperazine moieties adopted the chair conformation in the solid state (Figures S26 and S27), affording one-dimensional (1D) supramolecular polymers (LM)_n. When LM was protonated by HNO₃, the single-crystal structure of [LM•2H]²⁺•2NO₃⁻ (Figure 2A, middle) showed that pairs of diallylmelaminium were bridged by anion-dimers (NO₃⁻)₂, forming complementary (DDD-AAA)₂ hydrogen-bonded arrays with

¹Department of Chemistry, Dartmouth College, 41 College Street, Hanover 03755, USA

²United States Department of Energy, Ames Laboratory, 334 TASF Road, Ames, IA 50011, USA

³Department of Chemistry, Iowa State University, 2438 Pammel Drive, Ames, IA 50011, USA

⁴Key Laboratory of Green Preparation and Application for Functional Materials, Ministry of Education, School of Materials Science and Engineering, Hubei University, Wuhan 430062, P.R. China

⁵Department of Chemistry, Michigan State University, 578 S. Shaw Lane, East Lansing, MI 48824, USA

⁶Lead contact

*Correspondence:
wenlin.zhang@dartmouth.edu (W.Z.),
arossini@iastate.edu (A.J.R.),
chenfeng.ke@dartmouth.edu (C.K.)

<https://doi.org/10.1016/j.chempr.2021.11.014>

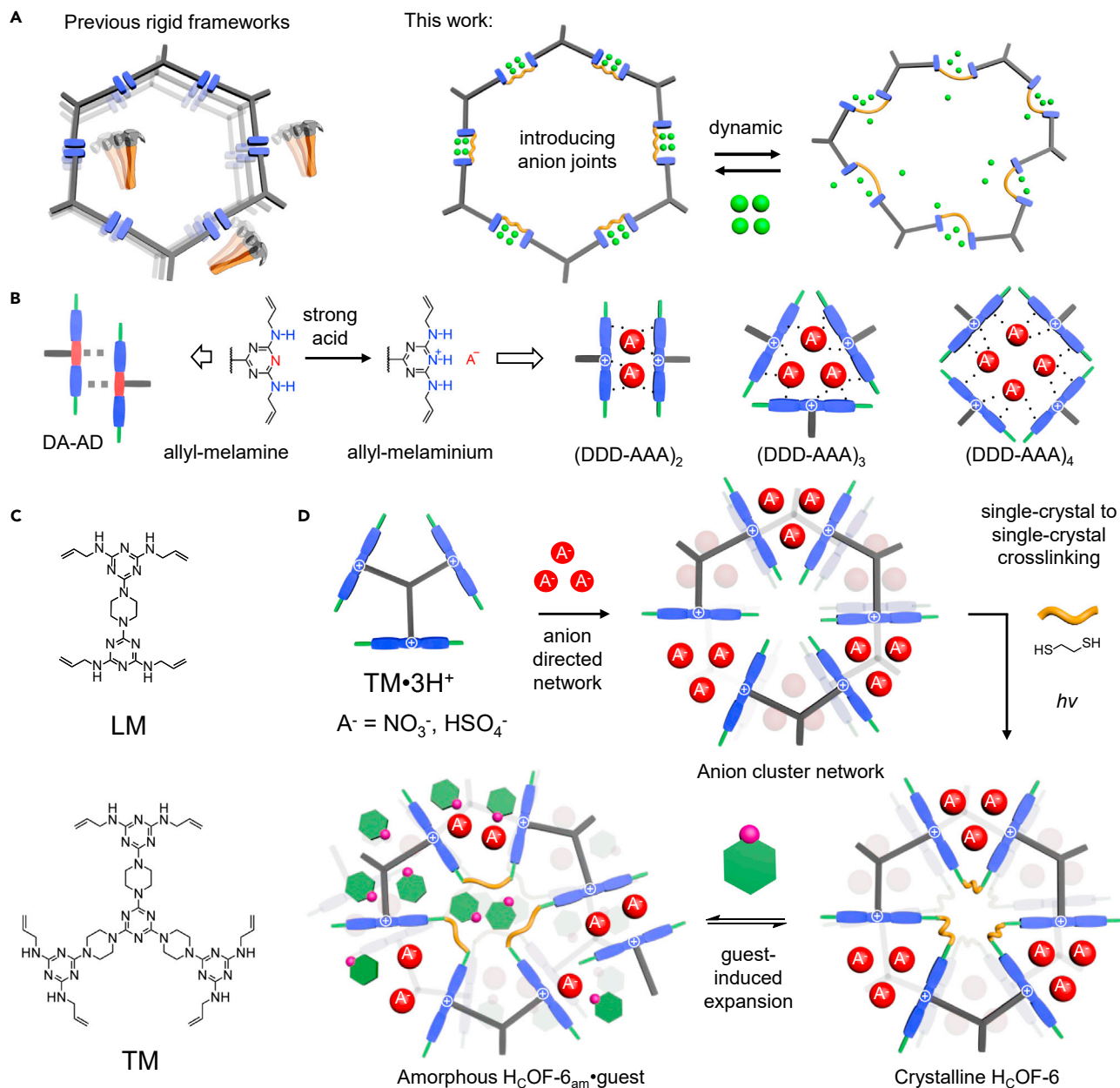


Figure 1. Design of anion cluster-based dynamic hydrogen-bonded cross-linked organic frameworks

(A) Comparison between traditional rigid organic frameworks and anion-cluster-directed organic frameworks with dynamic response reported in this work.

(B) Anion-directed formation of allyl-melaminium-based hydrogen-bonding arrays.

(C) Chemical structures of a LM and a TM.

(D) Illustration of the anion-cluster-directed formation of a hexagonal hydrogen-bonded network and the synthesis of $\text{H}_2\text{COF-6}$ through SCSC crosslinking. Upon guest sorption, $\text{H}_2\text{COF-6}$ exhibited (ir)reversible crystalline-to-amorphous dynamic expansions.

strong hydrogen bonds ($\text{N-H} \cdots \text{O-N} = 2.09, 2.10, \text{ and } 2.31 \text{ \AA}$, Figure S28). Mixing LM and H_2SO_4 afforded single crystals of $[\text{LM} \cdot 2\text{H}]^{2+} \cdot 2\text{HSO}_4^-$. In the solid state (Figure 2A, right), hydrogen-bonded anion-dimers³⁹ (HSO_4^-)₂ were found to bridge neighboring pairs of diallylmelaminiums of $[\text{LM} \cdot 2\text{H}]^{2+}$, forming $(\text{DDD-AAA})_2$ hydrogen-bonding arrays with even shorter hydrogen bonds ($\text{N-H} \cdots \text{O-S} = 1.99, 2.08, \text{ and } 2.14 \text{ \AA}$, Figure S30). These LM-based assemblies were closely packed

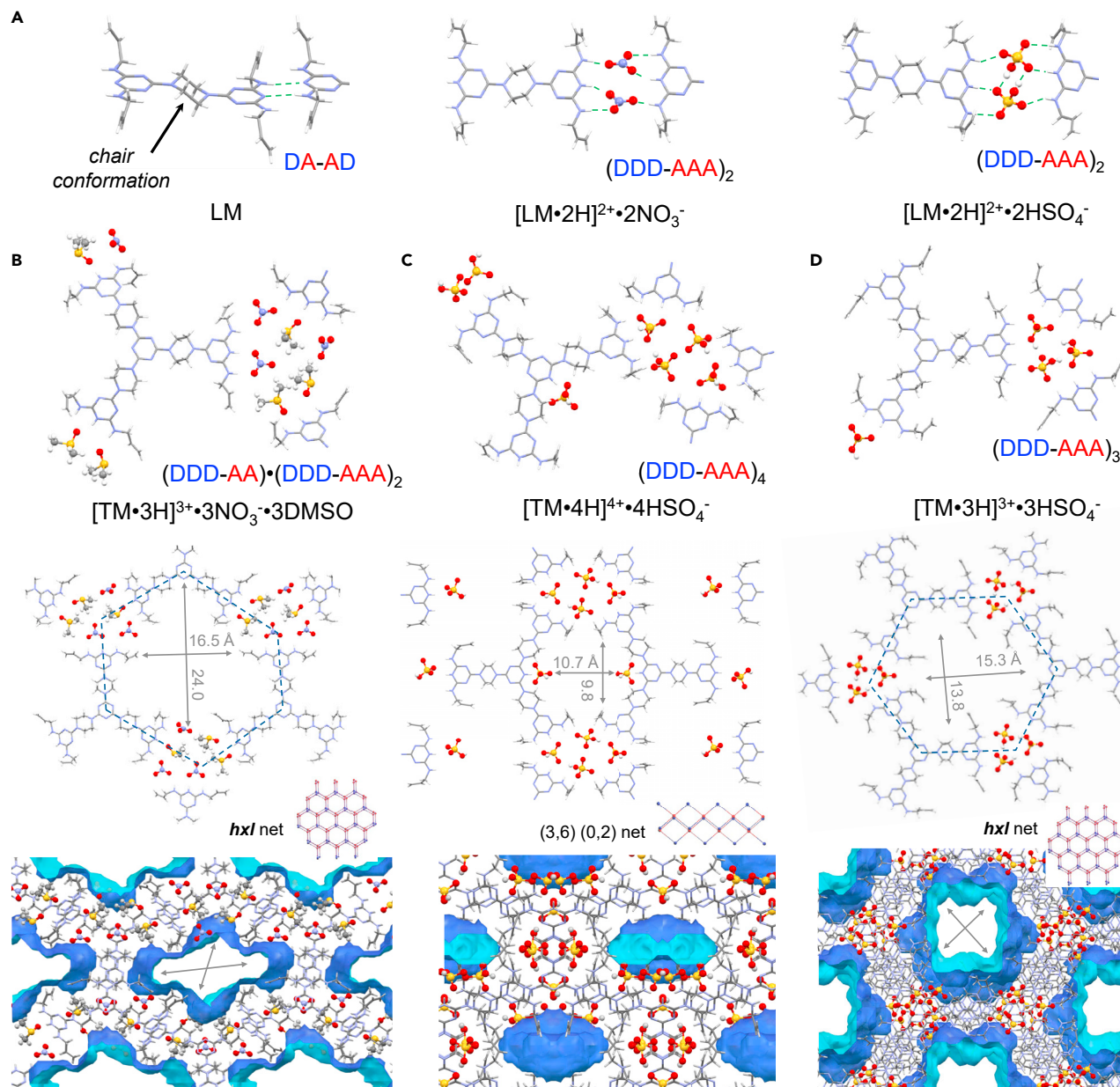


Figure 2. Crystal structure analyses

(A) Single-crystal X-ray structures of LM, $[LM\cdot 2H]^{2+}\cdot 2NO_3^-$, and $[LM\cdot 2H]^{2+}\cdot 2HSO_4^-$ with highlighted hydrogen-bonding arrays.

(B–D) Single-crystal X-ray structures of $[TM\cdot 3H]^{3+}\cdot 3NO_3^- \cdot 3DMSO$ (B), $[TM\cdot 4H]^{4+}\cdot 4HSO_4^-$ (C), and $[TM\cdot 3H]^{3+}\cdot 3HSO_4^-$ (D) depicted with different stacking models, respectively.

with no appreciable void space, and the chair-formed piperazine moieties prevented any strong π – π stacking (Figures S26–S31). The assembly of $[LM\cdot 2H]^{2+}\cdot 2NO_3^-$ and $[LM\cdot 2H]^{2+}\cdot 2HSO_4^-$ with complementary (DDD-AAA)₂ hydrogen-bonding arrays motivated us to synthesize a TM for H_cOF construction. TM was synthesized in four steps (Scheme S2): the mono-Boc-protection of piperazine, reaction with intermediate 2,4-diallylamino-6-chloro-1,3,5-triazine, followed by Boc-deprotection, and reaction with cyanuric chloride. Slow evaporation of a mixture of TM and fuming HNO₃ in dioxane-DMSO (v/v = 3:1) afforded single crystals of $[TM\cdot 3H]^{3+}\cdot 3NO_3^- \cdot 3DMSO$ in the monoclinic P2₁/n space group (Figure 2B).

$[\text{TM}\bullet\text{3H}]^{3+}\bullet\text{3NO}_3^-\bullet\text{3DMSO}$ formed a distorted hexagonal framework with solvent-occupied voids, featuring a pore size of $24.0 \times 16.5 \text{ \AA}$. The diallylmelaminium moieties of three $[\text{TM}\bullet\text{3H}]^{3+}$ were connected by a cluster of three NO_3^- anions and three DMSO (Figures 2B, top and S33). Unfortunately, due to the participation of DMSO in the cluster, the hydrogen-bonded network of $[\text{TM}\bullet\text{3H}]^{3+}\bullet\text{3NO}_3^-\bullet\text{3DMSO}$ is highly unstable, and crystallinity was lost upon solvent removal or exposure to dithiol cross-linkers.

When H_2SO_4 was mixed with TM, slow evaporation of the reaction mixture in dioxane-DMSO ($v/v = 2:1$) afforded single crystals of $[\text{TM}\bullet\text{4H}]^{4+}\bullet\text{4HSO}_4^-$ (Figure 2C) in the monoclinic $P2_1/n$ space group with unit cell parameters of $a = 13.6804(2)$, $b = 22.9165(4)$, $c = 20.7502(3) \text{ \AA}$, $\alpha = \gamma = 90^\circ$, $\beta = 102.646(2)^\circ$. Different from $[\text{TM}\bullet\text{3H}]^{3+}\bullet\text{3NO}_3^-\bullet\text{3DMSO}$, all four triazines of $[\text{TM}\bullet\text{4H}]^{4+}\bullet\text{4HSO}_4^-$ were protonated.⁴⁰ A unique rhombic tetrakis-anion cluster (HSO_4^-)₄ was discovered to bridge four diallylmelaminium moieties (Figure 2C), forming a 4-fold (DDD-AAA)₄ hydrogen-bonding array. In this tetrakis-anion cluster, individual HSO_4^- anions were stabilized by $\text{S}-\text{O}-\text{H}\cdots\text{O}-\text{S}$ hydrogen bonds, two of which also formed hydrogen bonds with the protonated central triazine of the $[\text{TM}\bullet\text{4H}]^{4+}$ ($\text{O}\cdots\text{H}-\text{N}^+ = 1.84 \text{ \AA}$, Figure S37) at the upper and lower layers. Surprisingly, only two out of the three diallylmelaminium arms of the $[\text{TM}\bullet\text{4H}]^{4+}$ participated in anion cluster formation, leaving one diallylmelaminium/ HSO_4^- ion-pair freely pointing toward the framework's void space (Figure 2C (middle)). Although the allyl groups of $[\text{TM}\bullet\text{4H}]^{4+}$ surmounted the voids, only 7% of discontinuous voids were measured in this hydrogen-bonded network (Figure 2C, bottom).

The existence of one non-participating diallylmelaminium in $[\text{TM}\bullet\text{4H}]^{4+}\bullet\text{4HSO}_4^-$ implied that there are other possible superstructures in the solid state. Therefore, we increased the crystallization temperature from room temperature to 80°C searching for a more stable network. After testing multiple solvent combinations for crystallization at 75°C – 80°C range (Table S1), single crystals of $[\text{TM}\bullet\text{3H}]^{3+}\bullet\text{3HSO}_4^-$ (Figure 2D) were successfully obtained at 80°C in a DMSO-nitrobenzene ($v/v = 1:3$) mixture. $[\text{TM}\bullet\text{3H}]^{3+}\bullet\text{3HSO}_4^-$ was crystallized in the monoclinic $C2$ space group with unit cell parameters of $a = 43.1933(15) \text{ \AA}$, $b = 23.2259(8) \text{ \AA}$, $c = 22.9907(5)$, $\alpha = \gamma = 90^\circ$, $\beta = 91.430(2)^\circ$. In this hexagonal hydrogen-bonded network (Figure 2D), a tris-anion cluster (HSO_4^-)₃ was discovered to bridge three diallylmelaminium units, forming a complementary 3-fold (DDD-AAA)₃ hydrogen-bonding arrays with hydrogen bond distances ranging between 1.81 – 2.14 \AA (Figure S43A). $[\text{TM}\bullet\text{3H}]^{3+}$ and (HSO_4^-)₃ clusters were packed alternatively along the c -axis, stabilizing the hydrogen-bonded 2D hexagonal networks through weak π - π , anion- π , and CH- π interactions (Figure S43B). Linear hexagonal channels of void in $[\text{TM}\bullet\text{3H}]^{3+}\bullet\text{3HSO}_4^-$ were measured to have a pore size diameter of $15.3 \times 13.8 \text{ \AA}$, and allyl groups decorated the pore surfaces (Figures 2D and S44).

To probe the reactivity and accessibility of the allyl groups in $[\text{TM}\bullet\text{4H}]^{4+}\bullet\text{4HSO}_4^-$ and $[\text{TM}\bullet\text{3H}]^{3+}\bullet\text{3HSO}_4^-$, ethanethiol (ET) was diffused into these single crystals followed by photo-irradiation (Scheme S3). The formed thioether products were dissolved in DMSO- d_6 for ^1H NMR analysis. The measured thiol-to-thioether conversions (Table S2) showed that only 55% of the allyl groups were consumed in $[\text{TM}\bullet\text{4H}]^{4+}\bullet\text{4HSO}_4^-$ due to the small discontinuous voids, whereas a complete thioether conversion was achieved in $[\text{TM}\bullet\text{3H}]^{3+}\bullet\text{3HSO}_4^-$ (Figure S12). When the ethanedithiol (EDT) cross-linker was employed, an incomplete thiol-to-thioether conversion was again observed in the cross-linked crystalline $\text{H}_c\text{OF-5}$ (Figures S14–S18). 2D $^1\text{H} \rightarrow ^{13}\text{C}$ cross-polarization heteronuclear correlation (CP-HETCOR) magic-angle spinning (MAS) solid-state NMR spectra of $\text{H}_c\text{OF-5}$ confirmed the presence of

unreacted allyl groups (Figure S17). Direct excitation ^{13}C NMR spectra revealed that only ca. 70% of the allyl groups were cross-linked (Table S3 and Figure S16).

Photo-cross-linking EDT-diffused single crystals of $[\text{TM}\bullet\text{3H}]^{3+}\bullet\text{3HSO}_4^-$ afforded single-crystalline $\text{H}_2\text{C}(\text{O})\text{F}-6$. When $[\text{TM}\bullet\text{3H}]^{3+}\bullet\text{3HSO}_4^-$ crystals were soaked in neat EDT, elemental analysis revealed that an excess of EDT (EDT: TM \approx 4:1) was attached to the allyl groups in the product (Table S4). Hence, the synthesis of $\text{H}_2\text{C}(\text{O})\text{F}-6$ was optimized by gradually reducing the amount of EDT until a nearly stoichiometric thiol-to-thioether conversion was reached in the elemental analysis (EDT: TM = 3.05–3.10: 1, Table S4). Comparison of 2D $^1\text{H} \rightarrow ^{13}\text{C}$ CP-HETCOR solid-state NMR spectra of $\text{H}_2\text{C}(\text{O})\text{F}-6$ recorded with short (0.1 ms) or long (2.0 ms) CP contact times (Figures 3D and S22) enabled the complete assignment of all ^1H and ^{13}C NMR signals (Figures 3B–3D). No appreciable olefin ^1H or ^{13}C NMR signals were observed in the 1D direct excitation ^1H , $^1\text{H} \rightarrow ^{13}\text{C}$ cross-polarization MAS (CPMAS) and direct excitation ^{13}C solid-state NMR spectra (Figures S20–S23) of $\text{H}_2\text{C}(\text{O})\text{F}-6$, confirming the complete consumption of all allyl groups upon photo-cross-linking. New ^{13}C and ^1H NMR signals emerged in the solid-state NMR spectra of $\text{H}_2\text{C}(\text{O})\text{F}-6$ at 20–40 and 1–3 ppm, respectively, confirming the formation of thioether cross-linking moieties. Compared with the solution phase ^1H NMR spectrum of $[\text{TM}\bullet\text{3H}]^{3+}\bullet\text{3HSO}_4^-$ (Figure 3C), the proton resonances of triazinium ($^+\text{N}-\text{H}$) and amine ($\text{N}-\text{H}$) of $\text{H}_2\text{C}(\text{O})\text{F}-6$ were shifted downfield (Figure 3D), indicating the deshielding effect of the tris-anion cluster in the solid state. After cross-linking, the olefin stretching and bending bands of $\text{H}_2\text{C}(\text{O})\text{F}-6$ at 1,500 and 900 cm^{-1} disappeared, and no free thiol vibrational band was observed in the IR spectrum (Figure 3E), further supporting a complete allyl-to-thioether conversion.

Powder X-ray diffraction (PXRD, Figure 3H) analysis showed that $\text{H}_2\text{C}(\text{O})\text{F}-6$ maintained high crystallinity, which is consistent with the ^{13}C solid-state NMR spectra that show relatively narrow ^{13}C NMR signals for the triazinium carbon atoms. The single-crystalline morphology of $\text{H}_2\text{C}(\text{O})\text{F}-6$ was observed in SEM and TEM analysis (Figures 3F and 3G). In the vapor sorption analysis (Figure 3I), supercritical CO_2 -activated $\text{H}_2\text{C}(\text{O})\text{F}-6$ adsorbed 103 cm^3/g STP of water, 105 cm^3/g STP of methanol, and 46 cm^3/g STP of toluene at 296 K, respectively, demonstrating its permanent porosity after solvent removal. Observation with an optical microscope revealed that large crystals of $[\text{TM}\bullet\text{3H}]^{3+}\bullet\text{3HSO}_4^-$ were shattered into layers of transparent smaller crystals of $\text{H}_2\text{C}(\text{O})\text{F}-6$ (Figure 3A) after photo-cross-linking. Single-crystal X-ray diffraction (SXRD) analysis showed that the monoclinic $[\text{TM}\bullet\text{3H}]^{3+}\bullet\text{3HSO}_4^-$ crystals were reconfigured to hexagonal $\text{H}_2\text{C}(\text{O})\text{F}-6$ crystals in the P3_121 space group with the cell unit parameters of $a = b = 24.0599(11)$ Å, $c = 22.9674(9)$, $\alpha = \beta = 90^\circ$, $\gamma = 120^\circ$. Anisotropic refinement of the backbone of $\text{H}_2\text{C}(\text{O})\text{F}-6$, which consists of $[\text{TM}\bullet\text{3H}]^{3+}$ and $(\text{HSO}_4^-)_3$ cluster (Figure 3J), showed that TM moieties in $\text{H}_2\text{C}(\text{O})\text{F}-6$ possessed similar conformations to its crystalline precursor $[\text{TM}\bullet\text{3H}]^{3+}\bullet\text{3HSO}_4^-$. $\text{H}_2\text{C}(\text{O})\text{F}-6$ retained distorted 1D porous channels after cross-linking (Figure 3K). The $(\text{HSO}_4^-)_3$ cluster was stabilized by the shallow bowl-shaped cavity of the $[\text{TM}\bullet\text{3H}]^{3+}$ moiety at the lower layer through multivalent anion- π interactions (Figure 3L). However, the flexible dithioether moieties in $\text{H}_2\text{C}(\text{O})\text{F}-6$ were heavily disordered in the crystal lattice, making unambiguous modeling of the thioether cross-linking motifs difficult (ball-stick in Figure 3J). To reveal the structural information of the flexible cross-linking moieties of $\text{H}_2\text{C}(\text{O})\text{F}-6$, we surveyed the nearby olefin group distances in the crystal precursor $[\text{TM}\bullet\text{3H}]^{3+}\bullet\text{3HSO}_4^-$ (Table S7; Figures S46 and S47). The distances between the nearby olefin groups suggested that the EDT cross-linking could either take place in an intralayer fashion parallel to the a/b plane (Figure 3J) to yield a stacked 2D polymer, or in an interlayer manner between two

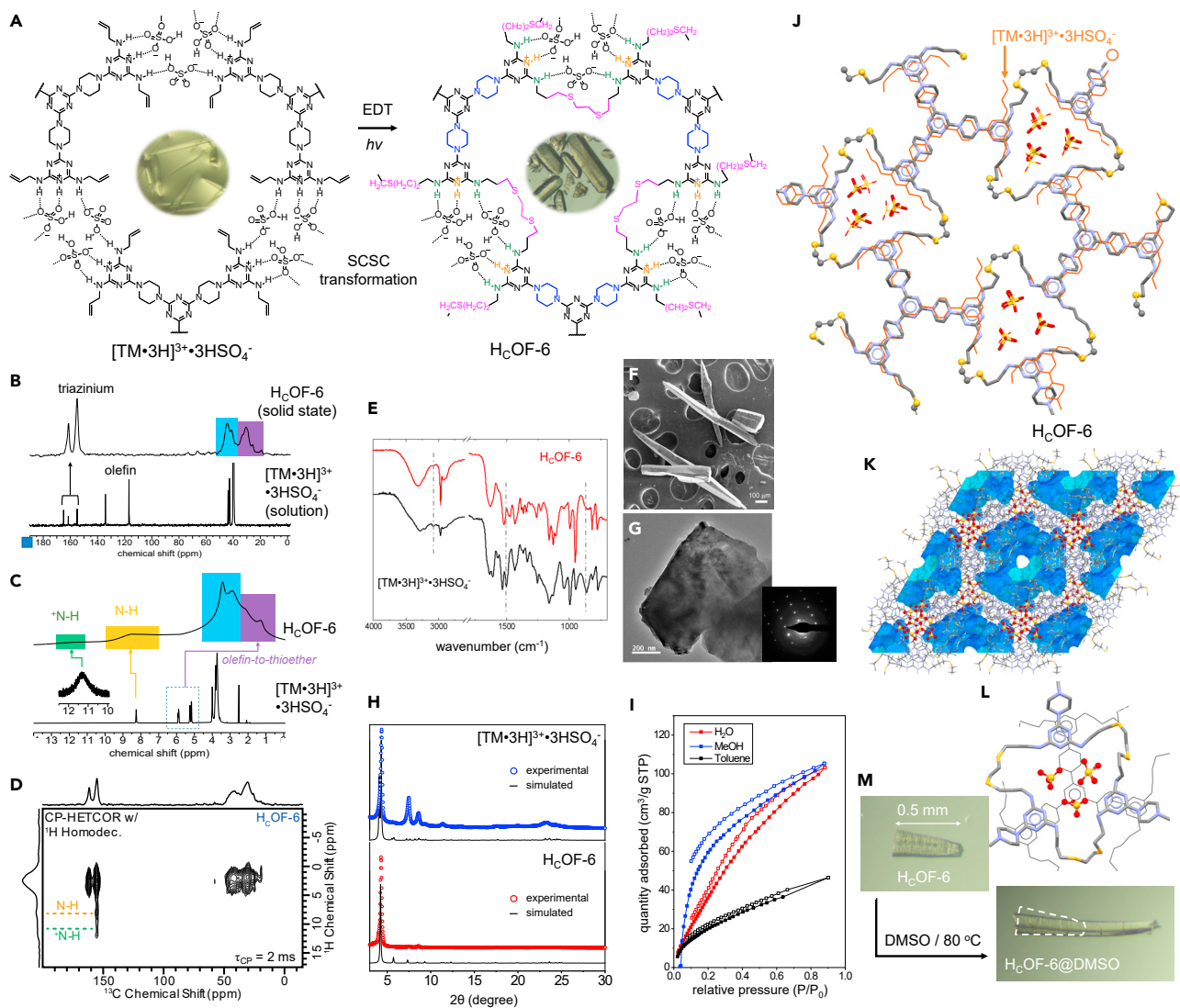


Figure 3. Synthesis and characterizations of single-crystalline H_cOF-6

(A) Synthesis of H_cOF-6 through thiol-ene SCSC transformation.

(B) Comparison of a (upper) 1D ¹H → ¹³C CPMAS solid-state NMR spectrum of H_cOF-6 recorded with 8.928 kHz MAS and (lower) a direct excitation ¹³C solution NMR spectrum of [TM•3H]³⁺•3HSO₄⁻ in DMSO-*d*₆.

(C) Comparison of a (upper) 1D ¹H spin-echo solid-state NMR spectrum of H_cOF-6 recorded with 50 kHz MAS and a (lower) ¹H solution NMR spectrum of [TM•3H]³⁺•3HSO₄⁻ in DMSO-*d*₆.

(D) 2D ¹H → ¹³C CP-HETCOR NMR spectrum of H_cOF-6 recorded with eDUMBO₁₋₂₂ ¹H homonuclear dipolar decoupling,⁴¹ a 2 ms CP contact time and 8.928 kHz MAS. (B–D) All NMR spectra were recorded at room temperature (~300 K).

(E) IR spectra of [TM•3H]³⁺•3HSO₄⁻ and H_cOF-6.

(F and G) SEM and TEM images of H_cOF-6, respectively. Inset: electron diffraction pattern of the TEM image.

(H) Experimental and simulated PXRD profiles of [TM•3H]³⁺•3HSO₄⁻ (blue) and H_cOF-6 (red).

(I) Vapor sorption isotherms (water, methanol, and toluene) of supercritical CO₂ activated H_cOF-6 recorded at 296 K.

(J) Overlaid structures of [TM•3H]³⁺•3HSO₄⁻ (orange color, wireframe) and H_cOF-6 (capped sticks). The dithioether moieties (ball-stick) were modeled to show the proposed intralayer cross-linking network. Hydrogen atoms were omitted for clarity.

(K) Packed structure and voids of H_cOF-6.

(L) The anion cluster and cross-linked DAM-H⁺ moieties in H_cOF-6.

(M) Images of a H_cOF-6 crystal (upper) before and (lower) after expansion induced by soaking in DMSO at 80°C for 24 h and then cooling to room temperature.

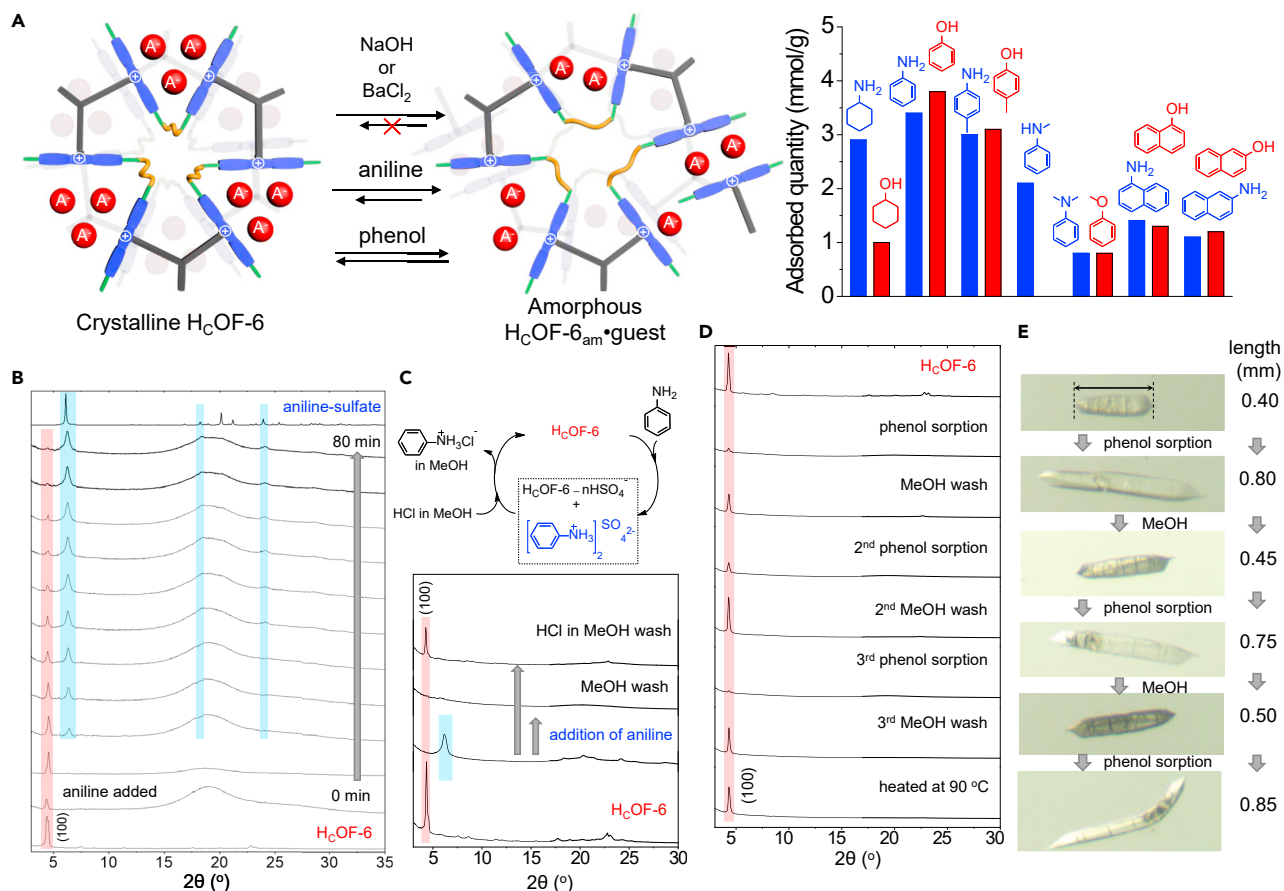


Figure 4. Dynamic guest sorption in H_cOF-6

- (A) Illustration of H_cOF-6's dynamic expansion upon adsorption of various guests and H_cOF-6's guest uptake capacities.
 (B) Time-dependent PXRD profiles of H_cOF-6 upon aniline addition. Crystalline aniline sulfate nanocrystals were formed in the expanded framework.
 (C) PXRD investigations of the crystallinity recovery of H_cOF-6_{am}•(PhNH₃)⁺₂SO₄²⁻ upon MeOH or HCl/MeOH washing.
 (D) PXRD profiles of H_cOF-6 upon three cycles of phenol uptake and contraction upon MeOH washing.
 (E) Images of a H_cOF-6 single crystal upon three cycles of phenol uptake and MeOH washing.

neighboring layers to yield a 3D cross-linked network (Figures S49–S58), or a mixture of both. Since our previous investigation demonstrated that the macroscopic crystal expansion of H_cOFs could reflect their cross-linking topology,²⁵ crystals of H_cOF-6 were soaked in DMSO at 80°C to dismantle its hydrogen-bonded network for crystal expansion (Figure 3M). The H_cOF-6•DMSO turned amorphous (Figure S60) and anisotropically expanded along the *c*-axis direction to more than twice its original size while shrinking slightly along the *a/b* plane. The anisotropic size expansion of H_cOF-6 suggested that (1) the intralayer cross-linking is the predominant connection in H_cOF-6, which allowed the crystal to greatly expand along the *c*-axis and mildly contract along *a/b* plane, and (2) a small amount of interlayer cross-linking also existed as defects⁴² in H_cOF-6, which prevented the exfoliation of H_cOF-6 as 2D polymers.^{43–45}

Since the disruption of (HSO₄⁻)₃ clusters in H_cOF-6 could give rise to dynamic framework expansion, the stability of H_cOF-6 was investigated against aqueous NaOH and BaCl₂/HCl (Figure 4A; Scheme S5). After soaking in these aqueous solutions, the HSO₄⁻ anions were extracted from the framework to afford crystal-like but amorphous polymer H_cOF-6_{am} (Figure S63). Re-protonation of the H_cOF-6_{am} using

H₂SO₄ or HCl/NaHSO₄ solutions did not regenerate crystalline H_COF-6. Interestingly, when the organic base aniline was employed, the H_COF-6 crystal expanded along the *c*-axis direction rapidly to more than twice its original length in 15–20 min at room temperature (Figure S65; Video S1). The dynamic size expansion was much faster and more extensive than H_COF-6 in a NaOH methanolic solution (~130%, 96 h, Figure S61). Time-dependent PXRD analysis (Figure 4B) showed that H_COF-6 gradually turned amorphous upon aniline adsorption. Meanwhile, a new set of diffraction peaks emerged, which closely matched the PXRD profile of aniline sulfate.⁴⁶ This result suggested that the adsorbed aniline in H_COF-6 was protonated by HSO₄⁻ to form nano-crystalline aniline sulfate. ¹H NMR desorption analysis revealed that 0.32 g/g (3.4 mmol/g) aniline was adsorbed (Figure 4A) and H_COF-6 was converted into H_COF-6_{am}•(PhNH₃)⁺₂SO₄²⁻. During the adsorption process, the crystallinity exchange took place between H_COF-6 and the *in situ* formed aniline sulfate, and the process was also partially reversible. When H_COF-6_{am}•(PhNH₃)⁺₂SO₄²⁻ was soaked in an HCl methanolic solution, the amorphous H_COF-6_{am}•(PhNH₃)⁺₂SO₄²⁻ was partially converted to crystalline H_COF-6 (Figure 4C). The regeneration of the H_COF-6 crystalline framework was attributed to the *in situ* reverse ion exchange from the locally crystallized aniline sulfate, which seeded the ordered (HSO₄⁻)₃ reformation. In contrast, when the aniline sulfate nanocrystals in H_COF-6_{am}•(PhNH₃)⁺₂SO₄²⁻ were removed by methanol washing, and the sample was then re-subjected to either H₂SO₄ or HCl/NaHSO₄ solutions, the crystallinity of H_COF-6 was not recovered (Figure S67). These observations indicated that the transfer of entropy between aniline and highly ordered H_COF-6 enabled the reversible crystallinity exchange, which also explains some of the unsuccessful attempts⁴⁷ to regenerate crystalline MOFs after demetallation and re-metallation cycles.

In the solutions of aniline analogs, such as cyclohexylamine, *p*-toluidine, and *N*-methylaniline (Figure 4A), H_COF-6 also dynamically expanded its dormant void space and adsorbed 2.9, 3.0, and 2.1 mmol/g at room temperature, respectively (Table S8). In contrast, when *N,N*-dimethylaniline (DMA) was used, H_COF-6 retained its crystallinity (Figure S68) and only adsorbed 0.7 mmol/g of DMA, despite its similar *p*K_b value to others.⁴⁸ Since DMA lacks hydrogen-bond donating groups, we suspect that the disruption of the tris-anion clusters in H_COF-6 using aniline and its analogs might be attributed to their hydrogen-bonding N–H groups more than their basicity. To confirm this hypothesis, H_COF-6's adsorption capabilities on an acidic substrate phenol and its analogs cyclohexanol, *p*-cresol, anisole, 1- and 2-naphthol were investigated (Figure 4A). H_COF-6 was immersed in concentrated dioxane solutions of these substrates, and the uptake capacities were measured by desorption ¹H NMR analysis (Table S9). Among them, only the adsorption of phenol and *p*-cresol in H_COF-6 resulted in significant crystalline-to-amorphous phase transformations, suggesting that both the substrates' chemical (hydrogen bonding) and physical (size) properties affect the framework dynamics.

In a concentrated phenol solution, H_COF-6 crystals rapidly expanded their sizes along the *c*-axis direction to more than twice the original length in about 40 min at room temperature (Figure 4E; Video S2). The phase change from crystalline H_COF-6 to amorphous H_COF-6_{am}•PhOH was clearly visualized (Video S2; Figures S70 and S71). The phenol adsorption-induced crystalline-to-amorphous phase transformation is highly reversible between the crystalline H_COF-6 and amorphous H_COF-6_{am}•PhOH (Figures 4D and 4E). When H_COF-6_{am}•PhOH was washed by MeOH, the sample size quickly shrunk via phenol desorption (Figure 4E). In a parallel PXRD experiment (Figure 4D), the amorphous sample recovered its crystallinity and

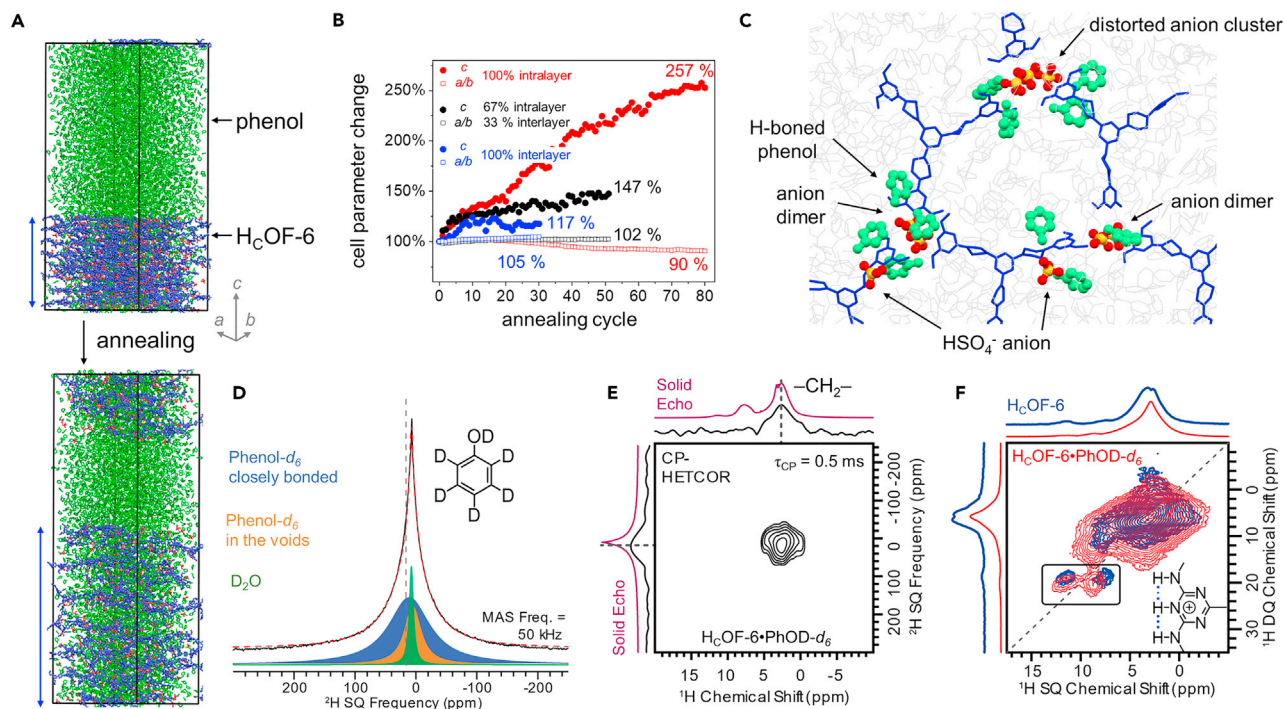


Figure 5. Molecular dynamics and NMR investigations of the dynamic nature of H_cOF-6

(A) MD snapshots of a supercell (initial: $6.1 \times 6.1 \times 6.8 \text{ nm}^3$) of H_cOF-6 constructed with intralayer cross-linking in a phenolic solution before (top) and after (bottom) thermal-assisted annealing. HSO₄⁻ anions (red) in H_cOF-6 (blue) and phenol (green) were color-coded, respectively.

(B) Supercell dimensions of interlayer and intralayer cross-linked H_cOF-6 measured in thermal-assisted annealing cycles (final cell size for intralayer H_cOF-6: $5.4 \times 5.4 \times 17.3 \text{ nm}^3$).

(C) A snapshot of a layer of the expanded H_cOF-6_{am}•PhOH. Hydrogen atoms were omitted for clarity.

(D) 1D ²H solid echo ($\pi/2$ - τ - $\pi/2$ - τ) solid-state NMR spectrum of H_cOF-6_{am}•PhOH-*d*₆. The experimental spectrum (black) was deconvoluted by fitting to three Gaussian-Lorentzian peaks.

(E) 2D ²H → ¹H CP-HETCOR NMR spectrum of H_cOF-6_{am}•PhOH-*d*₆ recorded with a 0.5 ms CP contact time.

(F) 2D ¹H dipolar DQ-SQ homonuclear correlation NMR spectra of H_cOF-6 (red) with and (blue) without phenol-*d*₆. All NMR spectra were recorded at $B_0 = 9.4 \text{ T}$ with 50 kHz MAS.

converted back to H_cOF-6. Two more cycles of the phenol adsorption and desorption were repeated, and the crystal sample demonstrated reversible size expansion and contraction (Figures 4D and 4E; Video S2). Although H_cOF-6_{am}•PhOH appeared to be an amorphous material under the TEM (Figure S76), the hexagonal macroscale shape of the original crystal remained as revealed in SEM analysis (Figure S75) with a few cracks along the *c*-axis direction, supporting our suggested structure of H_cOF-6, which had small amounts of interlayer cross-links.

To reveal the origin of the phenol-induced anisotropic expansion, all-atom molecular dynamics (MD) simulations were performed on H_cOF-6 using the GROMACS package.⁴⁹ We constructed a supercell with a slab of 4,000 phenols placed on top of H_cOF-6 as the initial state, which consisted of $a \bullet b \bullet c = 3 \times 3 \times 16 [\text{TM} \bullet 3\text{H}]^{3+} \bullet 3\text{HSO}_4^-$ moieties (Figure 5A). Intralayer and interlayer dithioether cross-linking moieties were defined virtually (Figures 5A and S77–S80) using harmonic springs of a rest length of 0.6 nm and a spring constant of 1,200 kJ/mol/nm². H_cOF-6 virtual samples are cross-linked in 100% interlayer, 33% inter- and 67% intralayer, and 100% intralayer ratios, respectively. They were subjected to phenol adsorption through cycles of annealing (350 → 550 → 350 K).⁵⁰ After multiple cycles (≥ 30), the 100% interlayer cross-linked virtual sample demonstrated marginal size expansion in all dimensions (Figure 5B). The 67% intralayer cross-linked virtual sample showed moderate

c-axis expansions (<150%). In comparison, the 100% intralayer cross-linked virtual sample exhibited significant expansions (>250%) along the c-axis and mild contraction along the *a/b* plane, consistent with our suggested model, which had a predominantly intralayer cross-linked H_COF-6. In the phenol expanded H_COF-6 that are fully intralayer cross-linked, (HSO₄⁻)₃ clusters were dissociated into (HSO₄⁻)₂ anion dimers and HSO₄⁻ anions in which the melaminium/HSO₄⁻ ion pairs were further stabilized via hydrogen bonding interactions with phenol (Figure 5C). The disruption of the tris-anion clusters enabled phenol insertion between the layers of H_COF-6 to expand the network, activating dormant voids to host more phenols in this expanded network (Figure 5A).

To confirm these simulated results experimentally, H_COF-6_{am}•PhOH-*d*₆ (98% deuterated) was prepared for ²H solid-state NMR spectroscopy experiments. A direct excitation MAS (*v_r* = 50 kHz) ²H NMR spectrum (Figure 5D) of H_COF-6_{am}•PhOH-*d*₆ revealed multiple ²H NMR signals with similar isotropic chemical shifts (δ_{iso}) at ca. 5, 7, and 11 ppm but significantly different linewidths; narrow ²H NMR signals correspond to phenol-*d*₆ with fast motion, whereas broad ²H NMR signals likely correspond to phenol-*d*₆ with reduced motion. We note that all adsorbed phenol-*d*₆ contains some degree of motion (i.e., they are not static) as no spinning sidebands, which are indicative of a significant first-order quadrupolar coupling interaction were observed (Figure S74).^{51–53} A 2D ²H → ¹H CP-HETCOR NMR spectrum (Figure 5E) of H_COF-6_{am}•PhOH-*d*₆ revealed correlations between the broad ²H NMR signal centered at ca. 11 ppm and the CH₂ ¹H NMR signals of H_COF-6 at ca. 2–3 ppm, which confirmed that some adsorbed phenols were in close spatial proximity to the H_COF-6 framework. Comparison of 2D ¹H dipolar double-quantum-single-quantum (DQ-SQ) homonuclear correlation solid-state NMR spectra^{54,55} (Figure 5F) of H_COF-6 (blue) and H_COF-6_{am}•PhOH-*d*₆ (red) revealed similar N-H•••H-N⁺ off-diagonal correlations between the melaminium and amine ¹H signals, suggesting that the local environment of melaminium/HSO₄⁻ was only changed slightly after the formation of hydrogen bonds with the adsorbed phenols as indicated in the MD simulations.

DISCUSSION

In summary, we have successfully introduced deformable anion clusters to construct hydrogen-bonded networks and subsequently synthesized a dynamic hydrogen-bonded cross-linked organic framework H_COF-6 through a thiol-ene SCSC transformation. We discovered a rare rhombic tetrakis-anion cluster (HSO₄⁻)₄ and a triangle tris-anion cluster (HSO₄⁻)₃ in the assembled molecular crystals, the latter of which directed the formation of a hexagonally packed hydrogen-bonded network. Photo-cross-linking the crystal precursor [TM•3H]³⁺•3HSO₄⁻ afforded single-crystalline H_COF-6 with large voids. H_COF-6 exhibited rapid and reversible size expansion and contraction (>200%) upon guest uptake and switching between crystalline and amorphous phases. Molecular dynamics simulations and solid-state NMR experiments revealed that the fast size expansion of H_COF-6 is attributed to the guest-induced disruption of the anion cluster, which is highly reversible for substrates, such as phenol, and partially reversible for aniline. Our strategy of introducing anion clusters to direct the synthesis of H_COFs will not only expand the substrate scope for H_COFs and promote their dynamic responses, but this synthetic method will also be directly transferable to the synthesis of HOFs and other supramolecular assemblies. Furthermore, the guest-induced dynamic network expansion and contraction features of H_COF-6 demonstrated the potential to integrate the features of traditional elastic polymeric materials with rigid framework materials, which will provide unique sorption capabilities for separation and catalysis for the development of porous materials operated with low energy consumption.

EXPERIMENTAL PROCEDURES

Resource availability

Lead contact

Further information and requests for resources should be directed to and will be fulfilled by the lead contact, Chenfeng Ke (chenfeng.ke@dartmouth.edu).

Materials availability

All materials generated in this study are available from the lead contact without restriction.

Data and code availability

The X-ray crystallographic coordinates for structures reported in this study have been deposited at the Cambridge Crystallographic Data Centre (CCDC), under deposition numbers CCDC: 2075758–2075763 and 2078152. These data can be obtained free of charge from the CCDC via www.ccdc.cam.ac.uk/data_request/cif.

Crystallization of $[\text{TM}(\bullet\text{3H})]^{3+} \bullet 3\text{HSO}_4^-$

Single crystals of $[\text{TM}(\bullet\text{3H})]^{3+} \bullet 3\text{HSO}_4^-$ were obtained from a mixture of DMSO-nitrobenzene (2.5 mL, v/v = 1:3) solution containing TM (25 mg) and two drops of conc. H_2SO_4 (98%) were placed in a 20-mL scintillation vial and allowed to evaporate slowly at 80°C. Rhombic-shaped, colorless crystals appeared within 2 weeks. The surfaces of the crystals were washed by a mixture of 1:1 MeCN-MeOH solution three times to remove any by-products and were activated using supercritical CO_2 for the elemental analysis. IR (ν , cm^{-1}): 1,609 (S=O). Elemental analysis: for $[\text{C}_{42}\text{H}_{60}\text{N}_{24}] \bullet [\text{H}_2\text{SO}_4]_3 \bullet [\text{CO}_2]_{4.2}$ calculated C: 40.21% H: 4.82% N: 24.36% S: 6.97%, found C: 39.17% H: 4.94% N: 25.44% S: 5.89%.

Synthesis of $\text{H}_c\text{OF-6}$

Single crystals of $[\text{TM}(\bullet\text{3H})]^{3+} \bullet 3\text{HSO}_4^-$ were washed by a mixture of 3:1 MeCN-MeOH solution three times to remove any by-products. Single crystals samples (~30 mg) were taken in a 20-mL glass vial to which 1 mL MeCN and 0.02 mL EDT were added and kept overnight in the dark. The mixture was replaced with a fresh portion of 0.02 mL EDT and 1 mL MeCN after 24 h. The reaction vial was irradiated under the UV light (medium-pressure 175-watt Hg lamp) for 72 h with forced air cooling. The crystal samples were collected and washed by an excess of MeCN to remove the unreacted EDT. MeCN solvent-containing samples were used for single-crystal X-ray analysis. The crystal samples were activated using supercritical CO_2 three times and used for different analyses. Elemental analysis: formula $[\text{C}_{42}\text{H}_{60}\text{N}_{24}] \bullet [\text{H}_2\text{SO}_4]_3 \bullet [\text{EDT}]_{3.1} \bullet [\text{CO}_2]_4$, calc: C 37.69%, H 5.13%, N 20.21%, S 17.73%, found: C 37.38%, H 5.45%, N 20.23%, S 17.89%. Solid-state ^{13}C NMR (100 MHz): 161.4, 155.1, 44.3, 41.5, 33.1, 30.7, 25.8.

Regeneration of the crystallinity of $\text{H}_c\text{OF-6}$

Regeneration of the $(\text{HSO}_4^-)_3$ anion clusters is critical for the reformation of crystalline $\text{H}_c\text{OF-6}$. Experimentally, $\text{H}_c\text{OF-6}$ sample (~5 mg) was placed on a non-diffracting PXRD plate, and its PXRD diffraction data were collected. Next, 30 μL of phenol was carefully added, immersing these crystals under liquid without spreading them out. The sample was kept still for approximately 15 min to allow extensive phenol adsorption. During this period, the plate was occasionally mounted on the instrument to check for crystallinity loss. Once the PXRD profile was almost lost, as shown further on, the excess of phenol was carefully removed by filter paper without disturbing the crystals. Thereafter, a MeOH solution (~100 μL) was gently added to

the crystals. The mixture was allowed to sit for 10 min, and PXRD data were collected. This procedure was repeated three times with the same sample.

Detailed procedures for the synthesis of monomers are described in the [supplemental information](#), and they are fully characterized by NMR spectroscopy and high-resolution electrospray ionization mass spectrometry.

SUPPLEMENTAL INFORMATION

Supplemental information can be found online at <https://doi.org/10.1016/j.chempr.2021.11.014>.

ACKNOWLEDGMENTS

This work is supported by the National Science Foundation CAREER award (DMR-1844920). J.S. and C.K. thank the American Chemical Society Petroleum Research Fund (58377-DNI10) and the Beckman Foundation Beckman Young Investigator program. Solid-state NMR experiments and data analysis (R.W.D. and A.J.R.) were supported by the U.S. Department of Energy (DOE), Office of Science, Basic Energy Sciences, Materials Science, and Engineering Division. The Ames Laboratory is operated for the U.S. DOE by Iowa State University under contract no. DE-AC02-07CH11358. A.J.R. acknowledges additional support from the Alfred P. Sloan Foundation through a Sloan research fellowship. W.Z. thanks Dartmouth College for the startup fund and the Burke initiative award. Funding for the single-crystal X-ray diffractometer at MSU was provided by the MRI program by the National Science Foundation under grant No. 1919565. We thank Dr. Pierre Le Magueres at the Rigaku Americas Corporation and Dr. Simon Teat at the Advanced Light Source, Lawrence Berkeley National Lab, for their help with single-crystal data collection. We thank Dr. Ramalingam Natarajan, Principal scientist, CSIR-Indian Institute of Chemical Biology, India, for valuable discussion and help with the crystal structure refinement.

AUTHOR CONTRIBUTIONS

J.S. performed the synthesis and materials characterization under the supervision of C.K.; R.W.D. and A.J.R. performed the solid-state NMR spectroscopy experiments. W.Z. performed the MD simulations. X.J. initiated the project, and M.Z. performed some of the materials characterizations. R.S. collected the single-crystal data. The manuscript was drafted by C.K. with inputs from all co-authors.

DECLARATION OF INTERESTS

The authors declare no competing interests.

Received: July 16, 2021

Revised: September 14, 2021

Accepted: November 11, 2021

Published: December 7, 2021

REFERENCES

1. Krause, S., Hosono, N., and Kitagawa, S. (2020). Chemistry of soft porous crystals: structural dynamics and gas adsorption properties. *Angew. Chem. Int. Ed. Engl.* *59*, 15325–15341.
2. Le Ouay, B., Kitagawa, S., and Uemura, T. (2017). Opening of an accessible microporosity in an otherwise nonporous metal-organic framework by polymeric guests. *J. Am. Chem. Soc.* *139*, 7886–7892.
3. Serre, C., Mellot-Draznieks, C., Surblé, S., Audebrand, N., Filinchuk, Y., and Férey, G. (2007). Role of solvent-host interactions that lead to very large swelling of hybrid frameworks. *Science* *315*, 1828–1831.
4. Serre, C., Millange, F., Thouvenot, C., Noguès, M., Marsolier, G., Louër, D., and Férey, G. (2002). Very large breathing effect in the first nanoporous chromium (III)-based solids: MIL-53 or CrIII(OH)·{O₂C–C₆H₄–CO₂}·

- {HO₂C–C₆H₄–CO₂H}_x·H₂O_y. *J. Am. Chem. Soc.* **124**, 13519–13526.
- Diercks, C.S., and Yaghi, O.M. (2017). The atom, the molecule, and the covalent organic framework. *Science* **355**, eaal1585.
 - Jin, Y., Hu, Y., and Zhang, W. (2017). Tessellated multiporous two-dimensional covalent organic frameworks. *Nat. Rev. Chem.* **1**, 0056.
 - Bisbey, R.P., and Dichtel, W.R. (2017). Covalent organic frameworks as a platform for multidimensional polymerization. *ACS Cent. Sci.* **3**, 533–543.
 - Lohse, M.S., and Bein, T. (2018). Covalent organic frameworks: structures, synthesis, and applications. *Adv. Funct. Mater.* **28**, 1705553.
 - Geng, K., He, T., Liu, R., Dalapati, S., Tan, K.T., Li, Z., Tao, S., Gong, Y., Jiang, Q., and Jiang, D. (2020). Covalent organic frameworks: design, synthesis, and functions. *Chem. Rev.* **120**, 8814–8933.
 - Adachi, T., and Ward, M.D. (2016). Versatile and resilient hydrogen-bonded host frameworks. *Acc. Chem. Res.* **49**, 2669–2679.
 - Lin, R.B., He, Y., Li, P., Wang, H., Zhou, W., and Chen, B. (2019). Multifunctional porous hydrogen-bonded organic framework materials. *Chem. Soc. Rev.* **48**, 1362–1389.
 - Li, P., Ryder, M.R., and Stoddart, J.F. (2020). Hydrogen-bonded organic frameworks: a rising class of porous molecular materials. *Acc. Mater. Res.* **1**, 77–87.
 - Wang, B., Lin, R.B., Zhang, Z., Xiang, S., and Chen, B. (2020). Hydrogen-bonded organic frameworks as a tunable platform for functional materials. *J. Am. Chem. Soc.* **142**, 14399–14416.
 - Ma, Y.X., Li, Z.J., Wei, L., Ding, S.Y., Zhang, Y.B., and Wang, W. (2017). A dynamic three-dimensional covalent organic framework. *J. Am. Chem. Soc.* **139**, 4995–4998.
 - Chen, Y., Shi, Z.L., Wei, L., Zhou, B., Tan, J., Zhou, H.L., and Zhang, Y.B. (2019). Guest-dependent dynamics in a 3D covalent organic framework. *J. Am. Chem. Soc.* **141**, 3298–3303.
 - Zhu, Q., Wang, X., Clowes, R., Cui, P., Chen, L., Little, M.A., and Cooper, A.I. (2020). 3D cage COFs: a dynamic three-dimensional covalent organic framework with high-connectivity organic cage nodes. *J. Am. Chem. Soc.* **142**, 16842–16848.
 - Liu, X., Li, J., Gui, B., Lin, G., Fu, Q., Yin, S., Liu, X., Sun, J., and Wang, C. (2021). A crystalline three-dimensional covalent organic framework with flexible building blocks. *J. Am. Chem. Soc.* **143**, 2123–2129.
 - Wang, H., Li, B., Wu, H., Hu, T.L., Yao, Z., Zhou, W., Xiang, S., and Chen, B. (2015). A flexible microporous hydrogen-bonded organic framework for gas sorption and separation. *J. Am. Chem. Soc.* **137**, 9963–9970.
 - Cui, P., Svensson Grape, E., Spackman, P.R., Wu, Y., Clowes, R., Day, G.M., Inge, A.K., Little, M.A., and Cooper, A.I. (2020). An expandable hydrogen-bonded organic framework characterized by three-dimensional electron diffraction. *J. Am. Chem. Soc.* **142**, 12743–12750.
 - Huang, Q., Li, W., Mao, Z., Zhang, H., Li, Y., Ma, D., Wu, H., Zhao, J., Yang, Z., Zhang, Y., et al. (2021). Dynamic molecular weaving in a two-dimensional hydrogen-bonded organic framework. *Chem* **7**, 1321–1332.
 - Liu, Y., Ma, Y., Zhao, Y., Sun, X., Gándara, F., Furukawa, H., Liu, Z., Zhu, H., Zhu, C., Suenaga, K., et al. (2016). Weaving of organic threads into a crystalline covalent organic framework. *Science* **351**, 365–369.
 - Liu, Y., Ma, Y., Yang, J., Diercks, C.S., Tamura, N., Jin, F., and Yaghi, O.M. (2018). Molecular weaving of covalent organic frameworks for adaptive guest inclusion. *J. Am. Chem. Soc.* **140**, 16015–16019.
 - Brunet, P., Demers, E., Maris, T., Enright, G.D., and Wuest, J.D. (2003). Designing permeable molecular crystals that react with external agents to give crystalline products. *Angew. Chem. Int. Ed. Engl.* **42**, 5303–5306.
 - Lin, Y., Jiang, X., Kim, S.T., Alahakoon, S.B., Hou, X., Zhang, Z., Thompson, C.M., Smaldone, R.A., and Ke, C. (2017). An elastic hydrogen-bonded cross-linked organic framework for effective iodine capture in water. *J. Am. Chem. Soc.* **139**, 7172–7175.
 - Jiang, X., Cui, X., Duncan, A.J.E., Li, L., Hughes, R.P., Staples, R.J., Alexandrov, E.V., Proserpio, D.M., Wu, Y., and Ke, C. (2019). Topochemical synthesis of single-crystalline hydrogen-bonded cross-linked organic frameworks and their guest-induced elastic expansion. *J. Am. Chem. Soc.* **141**, 10915–10923.
 - Sattler, A., and Schnick, W. (2010). Melemium hydrogensulfate H₃C₆N₇(NH₂)₃(HSO₄)₃—the first triple protonation of melem. *Z. Anorg. Allg. Chem.* **636**, 2589–2594.
 - Hema, K., Ravi, A., Raju, C., Pathan, J.R., Rai, R., and Sureshan, K.M. (2021). Topochemical polymerizations for the solid-state synthesis of organic polymers. *Chem. Soc. Rev.* **50**, 4062–4099.
 - Hema, K., Ravi, A., Raju, C., and Sureshan, K.M. (2021). Polymers with advanced structural and supramolecular features synthesized through topochemical polymerization. *Chem. Sci.* **12**, 5361–5380.
 - Brekalo, I., Deliz, D.E., Barbour, L.J., Ward, M.D., Friščić, T., and Holman, K.T. (2020). Microporosity of a guanidinium organodisulfonate hydrogen-bonded framework. *Angew. Chem. Int. Ed. Engl.* **59**, 1997–2002.
 - Xing, G., Yan, T., Das, S., Ben, T., and Qiu, S. (2018). Synthesis of crystalline porous organic salts with high proton conductivity. *Angew. Chem. Int. Ed. Engl.* **57**, 5345–5349.
 - Xing, G., Bassanetti, I., Bracco, S., Negroni, M., Bezuïdenhout, C., Ben, T., Sozzani, P., and Comotti, A. (2019). A double helix of opposite charges to form channels with unique CO₂ selectivity and dynamics. *Chem. Sci.* **10**, 730–736.
 - Cullen, D.A., Gardiner, M.G., and White, N.G. (2019). A three dimensional hydrogen bonded organic framework assembled through antielectrostatic hydrogen bonds. *Chem. Commun. (Camb)* **55**, 12020–12023.
 - He, Q., Tu, P., and Sessler, J.L. (2018). Supramolecular chemistry of anionic dimers, trimers, tetramers and clusters. *Chem* **4**, 46–93.
 - Zhao, W., Flood, A.H., and White, N.G. (2020). Recognition and applications of anion-anion dimers based on anti-electrostatic hydrogen bonds (AEHBs). *Chem. Soc. Rev.* **49**, 7893–7906.
 - Vella-Zarb, L., Braga, D., Guy Orpen, A.G., and Baisch, U. (2014). The influence of hydrogen bonding on the planar arrangement of melamine in crystal structures of its solvates, cocrystals and salts. *CrystEngComm* **16**, 8147–8159.
 - Shinde, S.V., and Talukdar, P. (2017). A dimeric bis(melamine)-substituted bispidine for efficient transmembrane H⁺/Cl[−] cotransport. *Angew. Chem. Int. Ed. Engl.* **56**, 4238–4242.
 - Wei, M.-J., Gao, Y., Li, K., Li, B., Fu, J., Zang, H., Shao, K., and Su, Z. (2019). Supramolecular hydrogen-bonded organic networks through acid-base pairs as efficient proton-conducting electrolytes. *CrystEngComm* **21**, 4996–5001.
 - Amm, M., Platzer, N., Guilhem, J., Bouchet, J.P., and Volland, J.P. (1998). Structural and conformational study of substituted triazines by 15N NMR and X-ray analysis. *Magn. Reson. Chem.* **36**, 587–596.
 - Fatila, E.M., Twum, E.B., Sengupta, A., Pink, M., Karty, J.A., Raghavachari, K., and Flood, A.H. (2016). Anions stabilize each other inside macrocyclic hosts. *Angew. Chem. Int. Ed. Engl.* **55**, 14057–14062.
 - List, M., Puchinger, H., Gabriel, H., Monkowius, U., and Schwarzing, C. (2016). N-methylmelamines: synthesis, characterization, and physical properties. *J. Org. Chem.* **81**, 4066–4075.
 - Sakellariou, D., Lesage, A., Hodgkinson, P., and Emsley, L. (2000). Homonuclear dipolar decoupling in solid-state NMR using continuous phase modulation. *Chem. Phys. Lett.* **319**, 253–260.
 - August, D.P., Dryfe, R.A.W., Haigh, S.J., Kent, P.R.C., Leigh, D.A., Lemmonier, J.F., Li, Z., Murny, C.A., Palmer, L.I., Song, Y., et al. (2020). Self-assembly of a layered two-dimensional molecularly woven fabric. *Nature* **588**, 429–435.
 - Kory, M.J., Wörle, M., Weber, T., Payamyar, P., van de Poll, S.W., Dshemuchadse, J., Trapp, N., and Schlüter, A.D. (2014). Gram-scale synthesis of two-dimensional polymer crystals and their structure analysis by X-ray diffraction. *Nat. Chem.* **6**, 779–784.
 - Schlüter, A.D., Weber, T., and Hofer, G. (2020). How to use X-ray diffraction to elucidate 2D polymerization propagation in single crystals. *Chem. Soc. Rev.* **49**, 5140–5158.
 - Lange, R.Z., Synnatschke, K., Qi, H., Huber, N., Hofer, G., Liang, B., Huck, C., Pucci, A., Kaiser, U., Backes, C., and Schlüter, A.D. (2020). Enriching and quantifying porous single layer 2D polymers by exfoliation of chemically modified van der Waals crystals. *Angew. Chem. Int. Ed. Engl.* **59**, 5683–5695.
 - Matulková, I., Cihelka, J., Fejfarová, K., Dušek, M., Pojarová, M., Vaněk, P., Kroupa, J., Šála, M., Krupková, R., and Němec, I. (2011). Semi-organic salts of aniline with

- inorganic acids: prospective materials for the second harmonic generation. *CrystEngComm* **13**, 4131–4138.
47. Furukawa, Y., Ishiwata, T., Sugikawa, K., Kokado, K., and Sada, K. (2012). Nano- and microsized cubic gel particles from cyclodextrin metal–organic frameworks. *Angew. Chem. Int. Ed. Engl.* **51**, 10566–10569.
48. Zhang, S. (2012). A reliable and efficient first principles-based method for predicting pKa values. 4. Organic bases. *J. Comput. Chem.* **33**, 2469–2482.
49. Dodda, L.S., Cabeza de Vaca, I., Tirado-Rives, J., and Jorgensen, W.L. (2017). LigParGen web server: an automatic OPLS-AA parameter generator for organic ligands. *Nucleic Acids Res.* **45**, W331–W336.
50. Liu, J., Xu, Q., and Jiang, J. (2019). A molecular simulation protocol for swelling and organic solvent nanofiltration of polymer membranes. *J. Membr. Sci.* **573**, 639–646.
51. Jelinski, L.W., Sullivan, C.E., and Torchia, D.A. (1980). ²H NMR study of molecular motion in collagen fibrils. *Nature* **284**, 531–534.
52. Vugmeyster, L., and Ostrovsky, D. (2017). Static solid-state ²H NMR methods in studies of protein side-chain dynamics. *Prog. Nucl. Magn. Reson. Spectrosc.* **101**, 1–17.
53. Mizuno, M. (2018). Solid-state ²H NMR studies of molecular motion in functional materials. In *Experimental Approaches of NMR Spectroscopy* (Springer), pp. 341–364.
54. Feike, M., Demco, D.E., Graf, R., Gottwald, J., Hafner, S., and Spiess, H.W. (1996). Broadband multiple-quantum NMR spectroscopy. *J. Magn. Reson. A* **122**, 214–221.
55. Schnell, I., Lupulescu, A., Hafner, S., Demco, D.E., and Spiess, H.W. (1998). Resolution enhancement in multiple-quantum MAS NMR spectroscopy. *J. Magn. Reson.* **133**, 61–69.